Discrete-Time Modeling of High Power Asymmetric Half-Bridge LED Constant-Current Driver Controlled by Digital Current Mode

ZHIYONG QIAO [1,2], **SHUNLI WANG** [1,3], **(Student Member, IEEE)**, **RONGHAI WANG** [2], **YILE SHI** [1], **XIN XIONG** [1], **NAN ZHANG** [4], **AND ZHIGUI LIU** [1]

[1] School of Information Engineering, Southwest University of Science and Technology, Mianyang 621010, China
[2] Department of Information Engineering, Mianyang Polytechnic, Mianyang 621000, China
[3] Department of Energy Technology, Aalborg University, 9220 Aalborg, Denmark
[4] Mianyang Meike Electronic Equipment Company Ltd., Mianyang 621000, China

Corresponding authors: Zhigui Liu (liuzhigui@swust.edu.cn) and Shunli Wang (wangshunli1985@126.com)

ABSTRACT The high-power Asymmetric half-bridge Converter (AHBC) LED constant current driver controlled by digital current mode is a fourth-order system. Static operating point, parasitic resistance, load characteristics, sampling effect, modulation mode and loop delay will have great influence on its dynamic performance. In this paper, the small-signal pulse transfer function of the driver is established by the discrete-time modeling method for two operating points with three modulation modes of trailing-edge, leading-edge and double-edge. And, the effects of parasitic parameters, delay, sampling and load etc. are fully considered in modeling. For a large number of complex exponential matrix operations, the first order Taylor formula is used for approximate calculation after the coefficient matrix is obtained by substituting the data. Then, the designed average current mode compensators based on state-space averaging small-signal model(SSA) are used for analog and digital control, and the loop characteristics and control performance are analyzed. Simulation and experimental comparison results show that the proposed discrete-time model(DTM) can more accurately describe the characteristics of resonant peak, high-frequency dynamic and loop delay, and is very suitable for the design of high frequency digital controller.

INDEX TERMS AHB LED constant-current driver, digital current-programmed control, discrete-time modeling, modulation effect.

I. INTRODUCTION

LED light source has many advantages such as high efficiency, energy saving, long life, high reliability and environmental friendliness, so it has been widely used in indoor and outdoor lighting. With the continuous improvement of luminous flux and luminous efficiency, it is expanding to high-power applications such as street lamps, squares, airports and stadiums in an all-round and rapid way [1]–[3]. As LED light source is usually driven by a constant current, the quality of driver will affect the overall performance of the light source. And because that asymmetric half-bridge converter has features of high conversion efficiency, low voltage stress,

The associate editor coordinating the review of this manuscript and approving it for publication was Wen-Sheng Zhao.

constant frequency control, and a small capacitive filter [4], it has great advantages when applied to high-power LED driver [5]–[8].

For AHBC, the feedback gain of current mode control can be increased independently of the secondary resonance to achieve better closed-loop performance. There are three control modes, including Peak Current Control (PCC) [9], Average Current Control (ACC) [10] and Charge Balance Control (CBC) [11]. Among them, ACC is more conducive to the improvement of closed-loop performance of the converter [12]. Previous AHBC current mode control was mostly realized by analog method. Driven by the development trend of high frequency digitization, Dr. J.d. Van Wyk proposed the idea of full digital current mode control [13], which will be conducive to improving the anti-interference ability,

power density and intelligence level of LED power supply. However, digital design will be faced with the problem that time quantization [14] and amplitude quantization [15] make the control performance worse. Therefore, the establishment of a more accurate small-signal discrete model will be beneficial to the improvement of digital control performance when parasitic parameters, modulation effects, quantization effects and loop delay are taken into account comprehensively [16].

For AHBC, J. Sebastan established its continuous small-signal model using the average circuit method [17]. This average model can accurately reflect the low frequency dynamic characteristics of the converter, but it has a large error in describing the high frequency characteristics above 3kHz. In particular, the prediction of high frequency resonance peak is far from the actual measured value. Moreover, parasitic resistance has a great influence on dynamic performance. Since then, S. Abedinpour established the AHBC state-space averaging small-signal model(SSA) for voltage mode control considering parasitic resistance [18]. B. Hoi established a SSA of the converter for current mode control AHBC, considering disturbance factors such as input voltage, primary side duty ratio, transformer leakage inductance and load current [19]. The SSA has been widely used in the design of analog controllers and has obtained better closed-loop control performance. Based on this model, the discrete-average model(DAM) of the converter can be obtained by using the mapping theory and considering the effects of sampling, modulation and delay [20]. However, the DAM is not accurate enough to describe the dynamic characteristics of high frequency, and it can only adopt approximate methods to handle delay and quantization error, so the control performance is poor when it is used in the design of high frequency digital controller.

The discrete-time modeling aims at describing the dynamic characteristics of the sample waveforms of the converter. The piecewise concept was used to directly obtain the difference equation, and then the discrete-time model(DTM) was obtained through linearization [21]. DTM can accurately describe the high-frequency dynamic characteristics of the converter and is very suitable for the design of digital compensation controller for high frequency DC-DC converter. The main research results include modeling for low sampling rate [22], for considering loop delay effect [23], and for considering sampling at any time point [24] etc.. For the problem that matrix exponential derivation is too complex in the process of discrete-time modeling, Taylor's first term is often used for approximate calculation [25]. In 2018, LI X built DTMs of Buck, Boost and Buck-Boost based on low-pass characteristics and considering modulation effects. Then, the model is transformed to S-domain for closed-loop design and better control effect is achieved [26]. For Buck LED driver controlled by peak current mode, Leng Minrui established an improved third-order DTM. And, the stability analysis shows that the model is an effective and accurate small-signal model [27].

Unlike Buck, Boost and buck-boost converters, AHBC is a fourth-order system due to the existence of resonant circuit and output LC filter circuit. As to a large number of complex matrix exponential calculations, it is difficult to obtain the symbolic expression of the DTM even if the first order approximation is adopted. In this paper, the discrete-time modeling is used to model the AHBC LED constant-current driver controlled by digital current mode. In the process of modeling, parasitic parameters, modulation effects, sampling effects and load effects are considered comprehensively. The first order approximation is adopted to establish the discrete-time model corresponding to each static operating point directly into the data. Finally, comparative analysis will be carried out between the DTM and the DAM by simulation and experiment to verify the accuracy of the model.

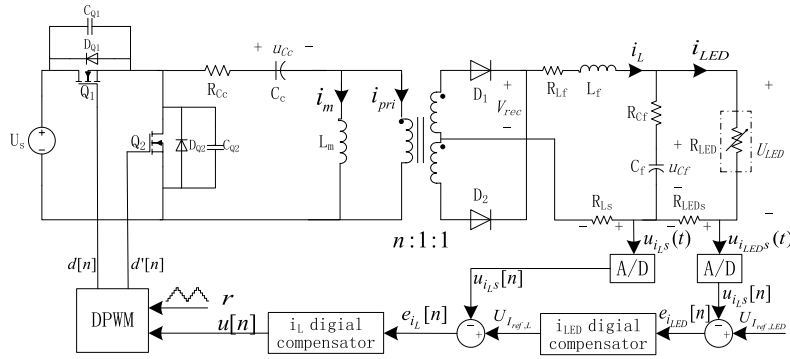## II. STATE-SPACE DESCRIPTION OF AHBC LED CONSTANT-CURRENT DRIVER

Figure 1 shows the digital current mode control loop of AHBC LED constant-current driver. It is composed of inductance current inner loop and LED current outer loop, including AHBC, LED, digital PWM, sampling holder, A/D converters and digital compensators. R_{LED} is the LED equivalent DC resistance at a specific operating point, which varies with operating point. R_{Cc}, R_{Cf} and R_{Lf} are equivalent parasitic resistances of C_m, L_f and C_f, while R_{Ls} and R_{LEDs} are sampling resistances of inductance current and LED current respectively.

The output of the i_{LED} digital compensator is the given value of the inductance current, $U_{I_{ref,L}}$. After $U_{I_{ref,L}}$ is compared with the inductance current obtained by high-speed sampling, the control signal $u[n]$ of the DPWM is calculated by the i_L digital controller, and then the duty ratio is adjusted to achieve the purpose of fast tracking the LED reference current. The outer loop is usually compensated by the digital PI regulator, and the inner loop can be controlled by the predictive current algorithm. The open-loop state-space description of AHBC LED constant-current driver without considering the control loop is shown in Equation (1).

$$\begin{cases} \dot{x} = d[\mathbf{A_1}x + \mathbf{B_1}\mathbf{u_s}] + d'[\mathbf{A_0}x + \mathbf{B_0}\mathbf{u_s}] \\ \mathbf{y} = d[\mathbf{C_1}x + \mathbf{E_1}\mathbf{u_s}] + d'[\mathbf{C_0}x + \mathbf{E_0}\mathbf{u_s}] \end{cases} \quad (1)$$

where, $\mathbf{x} = \begin{pmatrix} u_{Cc} & i_p & i_L & u_{Cf} \end{pmatrix}^T$ is the state variable, $\mathbf{y} = \begin{pmatrix} i_L & i_{LED} \end{pmatrix}^T$ is the output vector, $\mathbf{u_s}$ is the input vector, $\mathbf{A_i}$, $\mathbf{B_i}$, $\mathbf{C_i}$ and $\mathbf{E_i}$ are the state-space model of the converter subtopology, $i \in \{0, 1\}$ is the operating state, d and $d' = 1-d$ are the PWM continuous time control signal. The static operating point is shown in Equation (2).

$$\mathbf{X} = -\mathbf{A}^{-1}\mathbf{B}U_s = \begin{pmatrix} \dfrac{D}{2D(1-D)(1-2D)} \\ \dfrac{4D(1-D)R'_{C_c} + n^2(R'_{LED} + R_{L_f})}{2nD(1-D)} \\ \dfrac{4D(1-D)R'_{C_c} + n^2(R'_{LED} + R_{L_f})}{2nD(1-D)R'_{LED}} \\ \dfrac{2nD(1-D)R'_{LED}}{4D(1-D)R'_{C_c} + n^2(R'_{LED} + R_{L_f})} \end{pmatrix} U_s \quad (2)$$

FIGURE 1. Block diagram of AHBC LED constant-current driver by digital current mode control.

After adding the small-signal disturbance, removing the DC component and taking Laplace transform, the open-loop transfer function of state-space average small-signal from duty ratio to inductance current and LED current can be derived, as shown in Equation (3).

$$
\begin{cases}
G_{\hat{i}_L d}(s) = \dfrac{\hat{i}_L(s)}{\hat{d}(s)} \\
\quad \approx k_{id} \dfrac{(1+s/\omega_{cr})\left(1+s/(Q_{n1}\omega_{n1})+s^2/\omega_{n1}^2\right)}{\left(1+s/(Q_{d1}\omega_{d1})+s^2/\omega_{d1}^2\right)\left(1+s/Q_{d2}\omega_{d2}+s^2/\omega_{d2}^2\right)} \\
G_{\hat{i}_{LED} d}(s) = \dfrac{\hat{i}_{LED}(s)}{\hat{d}(s)} \\
\quad \approx k_{id} \dfrac{(1+s/\omega_{esr})\left(1+s/(Q_{n1}\omega_{n1})+s^2/\omega_{n1}^2\right)}{\left(1+s/(Q_{d1}\omega_{d1})+s^2/\omega_{d1}^2\right)\left(1+s/Q_{d2}\omega_{d2}+s^2/\omega_{d2}^2\right)}
\end{cases}
\tag{3}
$$

where,

$$
k_{id} = \frac{2(1-2D)U_s}{n(R'_{LED}+R'_{L_f})}, \qquad \omega_{esr} = \frac{1}{R_{C_f}C_f},
$$

$$
\omega_{cr} = \frac{1}{(R'_{LED}+R_{C_f})C_f}, \qquad \omega_{n1} = \sqrt{\frac{2}{L_m C_c}},
$$

$$
\omega_{d1} = \sqrt{\frac{1}{L_f C_f}}, \qquad \omega_{d2} = \sqrt{\frac{1}{L_m C_c}},
$$

$$
Q_{n1} = \frac{1}{\frac{2D(1-D)L_m}{n^2(R'_{LED}+R'_{L_f})}+R_{C_c}C_c}\,\omega_{n1}^{-1},
$$

$$
Q_{d1} = \frac{R'_{LED}+R'_{L_f}}{(R'_{LED}R'_{L_f}+R'_{L_f}R_{C_f}+R'_{LED}R_{C_f})C_f+L_f}\,\omega_{d1}^{-1},
$$

$$
Q_{d2} = \frac{1}{R_{C_c}C_c}\,\omega_{d2}^{-1}.
$$

This state-space average small-signal model fully considers the influence of parasitic parameters and load effect. It can well reflect the low-frequency dynamic characteristics of the converter. When it is applied to the design of the analog controller, a better control effect is achieved. However, sampling mode, loop delay, modulation effect and other factors are not taken into account in the establishment of the model, which is

one of the main reasons for the deterioration of digital control performance.

III. DISCRETE-TIME MODELING OF AHBC LED CONSTANT-CURRENT DRIVER

Without considering the small signal disturbance, the difference equation expression of static operating point of the converter is obtained by integrating equation (1), as shown in Equation (4).

$$
\begin{cases}
X((n+1)T_s) = (I - e^{\mathbf{A_1}DT_s}e^{\mathbf{A_0}D'T_s})^{-1} \\
\quad [-e^{\mathbf{A_1}(DT_s)}\mathbf{A_0^{-1}}(\mathbf{I}-e^{\mathbf{A_0}D'T_s})\mathbf{B_0}-\mathbf{A_1^{-1}}(\mathbf{I}-e^{\mathbf{A_1}T_s})\mathbf{B_1}]\mathbf{U_s} \\
Y((n+1)T_s) = \mathbf{C}(I - e^{\mathbf{A_1}DT_s}e^{\mathbf{A_0}D'T_s})^{-1} \\
\quad [-e^{\mathbf{A_1}(DT_s)}\mathbf{A_0^{-1}}(\mathbf{I}-e^{\mathbf{A_0}D'T_s})\mathbf{B_0}-\mathbf{A_1^{-1}}(\mathbf{I}-e^{\mathbf{A_1}T_s})\mathbf{B_1}] \\
\mathbf{U_s}+\mathbf{EU_s}
\end{cases}
\tag{4}
$$

PWM modulation of DC-DC converter includes three modes: trailing-edge, leading-edge and double-edge. As shown in Figure 2, in addition to the modulator itself inherent modulation delay, the sampling delay varied with the different modulation modes. For example, in the case of trailing-edge modulation, the inductance current is often sampled when the PWM is low, while with the double-edge modulation, the sample is often taken at the peak point of the triangular wave. Modulation delay and sampling delay are one of the main factors affecting the control performance of the converter. The influence degree varies with the delay time.

Different inductance current prediction algorithms can be formed according to different modulation modes, and then a variety of digital current prediction control strategies can be formed. Considering different modulation modes, the discrete-time modeling of the converter will be helpful to analyze, compare and optimize the design of these control strategies. In view of this point, discrete time models with three different modulation modes will be established below.

The sequence diagram and waveform of AHBC with trailing-edge modulation are shown in Figure 3. Sampling is carried out during $D = 0$, and $nt_{sampl} \sim (n+1)t_{sampl}$ is the switching period of Discrete-time modeling. Where, t_{sampl} is the sampling time point and t_d is the delay time including

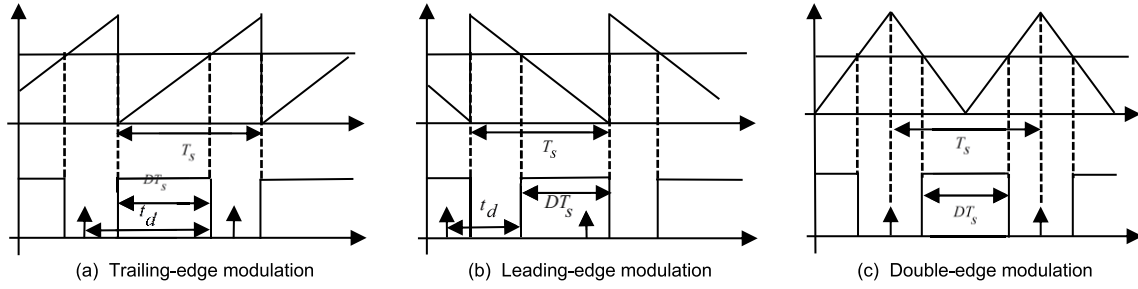**FIGURE 2.** Modulation method.

(a) Trailing-edge modulation (b) Leading-edge modulation (c) Double-edge modulation

TABLE 1. Discrete-time modeling of AHBC with trailing-edge modulation.

INTEGRAL INTERVAL	DIFFERENCE EQUATION	
$nT_s \sim nT_s + t_d - DT_s$	$\hat{\mathbf{x}}(nT_s + t_d - DT_s) = e^{\mathbf{A_0}(t_d - DT_s)}\hat{\mathbf{x}}(nT_s) + \int_{nT_s}^{nT_s + t_d - DT_s} e^{\mathbf{A_0}(nT_s + t_d - DT_s - \tau)}\mathbf{B_0}\hat{\mathbf{u}}(\tau)d\tau$	(5)
$nT_s + t_d - DT_s \sim nT_s + t_d + \hat{d}_n T_s$	$\hat{\mathbf{x}}(nT_s + t_d + \hat{d}_n T_s) = e^{\mathbf{A_1}(DT_s + \hat{d}_n T_s)}\hat{\mathbf{x}}(nT_s + t_d - DT_s) + \int_{nT_s + t_d - DT_s}^{nT_s + t_d} e^{\mathbf{A_1}(nT_s + t_d - \tau)}\mathbf{B_1}\hat{\mathbf{u}}(\tau)d\tau$ $+ \int_{nT_s + t_d}^{nT_s + t_d + \hat{d}_n T_s} e^{\mathbf{A_1}(nT_s + t_d + \hat{d}_n T_s - \tau)}\{\mathbf{B_1}\hat{\mathbf{u}}(\tau) + [(\mathbf{A_1} - \mathbf{A_0})\mathbf{X} + (\mathbf{B_1} - \mathbf{B_0})\mathbf{U}]\hat{d}(\tau)\}d\tau$	(6)
$nT_s + t_d + \hat{d}_n T_s \sim (n+1)T_s$	$\hat{\mathbf{x}}((n+1)T_s) = e^{\mathbf{A_0}(T_s - t_d - \hat{d}_n T)}\hat{\mathbf{x}}(nT_s + t_d + \hat{d}_n T_s) + \int_{nT_s + t_d + \hat{d}_n T_s}^{(n+1)T_s} e^{\mathbf{A_0}((n+1)T_s - \tau)}\mathbf{B_0}\hat{\mathbf{u}}(\tau)d\tau$	(7)
$\hat{\mathbf{x}}((n+1)T_s) = \underline{e^{\mathbf{A_0}(T_s - t_d - \hat{d}_n T)}e^{\mathbf{A_1}(DT_s + \hat{d}_n T_s)}e^{\mathbf{A_0}(t_d - DT_s)}\hat{\mathbf{x}}(nT_s)}$ $+ e^{\mathbf{A_0}(T_s - t_d - \hat{d}_n T)}e^{\mathbf{A_1}(DT_s + \hat{d}_n T_s)}\int_{nT_s}^{nT_s + t_d - DT_s} e^{\mathbf{A_0}(nT_s + t_d - DT_s - \tau)}\mathbf{B_0}\hat{\mathbf{u}}(\tau)d\tau + e^{\mathbf{A_0}(T_s - t_d - \hat{d}_n T)}\{\int_{nT_s + t_d - DT_s}^{nT_s + t_d} e^{\mathbf{A_1}(nT_s + t_d - \tau)}\mathbf{B_1}\hat{\mathbf{u}}(\tau)d\tau$ $+ \int_{nT_s + t_d}^{nT_s + t_d + \hat{d}_n T_s} e^{\mathbf{A_1}(nT_s + t_d + \hat{d}_n T_s - \tau)}\{\mathbf{B_1}\hat{\mathbf{u}}(\tau) + [(\mathbf{A_1} - \mathbf{A_0})\mathbf{X} + (\mathbf{B_1} - \mathbf{B_0})\mathbf{U}]\hat{d}(\tau)d\tau\} + \int_{nT_s + t_d + \hat{d}_n T_s}^{(n+1)T_s} e^{\mathbf{A_0}((n+1)T_s - \tau)}\mathbf{B_0}\hat{\mathbf{u}}(\tau)d\tau$	(8)	

sampling delay t_{ds}, calculated delay t_{dc} and modulation delay t_{dm}, $\hat{d}_n$ is the small duty cycle signal disturbance, and $x(n)$ is the state variable.

After small-signal disturbance is added and DC component is removed, the small-signal discrete-time model with trailing-edge modulation(DTMT) can be obtained by integrating the state-space equation in the interval of $nT_s \sim nT_s + t_d - DT_s$, $nT_s + t_d - DT_s \sim nT_s + t_d + \hat{d}_n T_s$ and $nT_s + t_d - DT_s \sim nT_s + t_d + \hat{d}_n T_s$ respectively, as shown in Formula (5) to Formula (7). And then, the difference equation of the converter can be obtained by substituting Formula (5) and Formula (6) into Formula (7), as shown in Formula (8).

For Formula (8), assuming no input disturbance, i.e. $\hat{u} = 0$, the difference equation of converter as shown in Equation (9) can be obtained.

$$\begin{cases} \hat{\mathbf{x}}[n+1] = \Phi\hat{\mathbf{x}}[n] + \gamma\hat{d}[n] \\ \hat{\mathbf{y}}[n+1] = \delta\hat{\mathbf{x}}[n+1] \end{cases} \quad (9)$$

TABLE 2 shows the coefficient matrix of the difference equation with modulation of Trailing-edge, Leading-edge (DTML) and Double-edge(DTMD) respectively.

After taking z transformation of Equation (9), the open-loop pulse transfer function shown in Formula (10) can be derived.

$$\mathbf{W(z)} = \frac{\hat{\mathbf{y}}(z)}{\hat{d}(z)} = \begin{bmatrix} G_{id}(z) = \dfrac{\hat{i}_L(z)}{\hat{d}(z)} \\ G_{ud}(z) = \dfrac{\hat{i}_{LED}(z)}{\hat{d}(z)} \end{bmatrix} = \mathbf{C_0}(z\mathbf{I} - \Phi)^{-1}\gamma \quad (10)$$

Sampling, delay, modulation and other influencing factors are taken into full account when the pulse transfer function is established by the discrete-time modeling method. Theoretically, the small-signal DTM can accurately represent the dynamic characteristics of the converter. However, to obtain the symbolic expression of the transfer function, a large number of complex matrix exponential operations are needed, and first-order Taylor expansion formula is often used for approximate calculation, as shown in Equation (11). But even
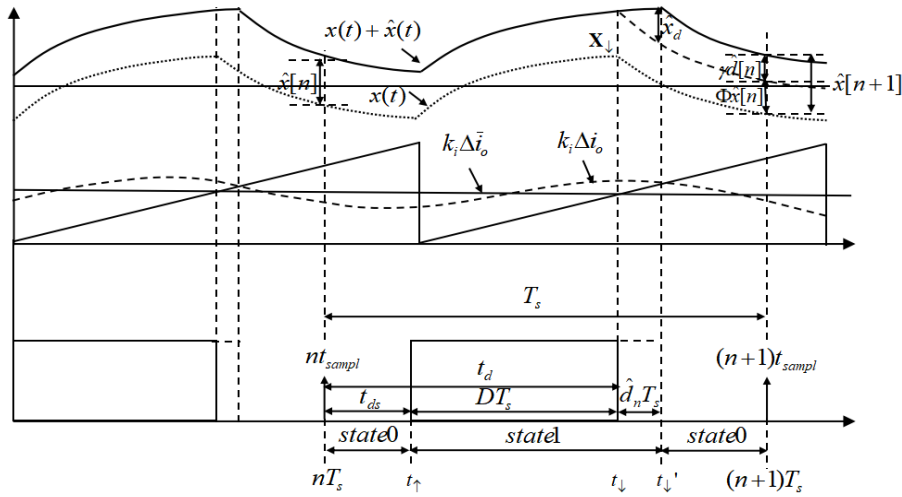
FIGURE 3. Sequence diagram and waveform of AHBC with trailing-edge modulation.

TABLE 2. Small-signal DTMs corresponding to different modulation modes.

DTMT	DTML	DTMD
$\mathbf{\Phi} = e^{\mathbf{A}_0(T_s - t_d)} e^{\mathbf{A}_1 DT_s} e^{\mathbf{A}_0(t_d - DT_s)}$	$\mathbf{\Phi} = e^{\mathbf{A}_1(t_d - D'T_s)} e^{\mathbf{A}_0 D'T_s} e^{\mathbf{A}_1(T_s - t_d)}$	$\mathbf{\Phi} = e^{\mathbf{A}_0 \frac{T_s}{2}(1-D)} e^{\mathbf{A}_1(DT_s)} e^{\mathbf{A}_0 \frac{T_s}{2}(1-D)}$
$\mathbf{\gamma} = T_s e^{\mathbf{A}_0(T_s - t_d)} \mathbf{F}_\downarrow$	$\mathbf{\gamma} = T_s e^{\mathbf{A}_0(T_s - t_d)} F_\uparrow$	$\mathbf{\gamma} = \frac{T_s}{2} e^{\mathbf{A}_0 \frac{T_s}{2}(1-D)} (\mathbf{F}_\downarrow + e^{\mathbf{A}_1 DT_s} \mathbf{F}_\uparrow)$
$\mathbf{\delta} = \mathbf{C}_0$	$\mathbf{\delta} = \mathbf{C}_1$	$\mathbf{\delta} = \mathbf{C}_0$

$$\mathbf{F}_\downarrow = [(\mathbf{A}_1 - \mathbf{A}_0)\mathbf{X}_\downarrow + (\mathbf{B}_1 - \mathbf{B}_0)\mathbf{U}], \quad \mathbf{F}_\uparrow = [(\mathbf{A}_1 - \mathbf{A}_0)\mathbf{X}_\uparrow + (\mathbf{B}_1 - \mathbf{B}_0)\mathbf{U}]$$

$$\mathbf{X}_\downarrow = (\mathbf{I} - e^{\mathbf{A}_1 DT_s} e^{\mathbf{A}_0 D'T_s})^{-1}[-e^{\mathbf{A}_1 DT_s} \mathbf{A}_0^{-1}(I - e^{\mathbf{A}_0 D'T_s})\mathbf{B}_0 - \mathbf{A}_1^{-1}(\mathbf{I} - e^{\mathbf{A}_1 DT_s})\mathbf{B}_1]\mathbf{U}$$

$$\mathbf{X}_\uparrow = e^{\mathbf{A}_0(D'T_s)}\mathbf{X}_\downarrow - \mathbf{A}_0^{-1}(I - e^{\mathbf{A}_0 D'T_s})\mathbf{B}_0 \mathbf{U}$$

so, for fourth-order systems, it is difficult to calculate the specific symbolic expression of the impulse transfer function, which is very inconvenient to analyze the relationship between converter parameters and system performance.

$$\mathbf{e}^{\mathbf{A}T} \approx \mathbf{I} - \mathbf{A}T \qquad (11)$$

IV. PARAMETER DESIGN AND ITS PULSE TRANSFER FUNCTION
A. PARAMETER DESIGN AND DUTY RATIO TO CURRENT PULSE TRANSFER FUNCTION
The driver is powered by 220V/50Hz AC, which is converted into 400V ($\pm$20%) DC by rectification and Boost PFC as the input of AHBC LED constant current driver. The hybrid module composed of 3×14 LEDs is selected as the load. The LED is XP-G2 R5 from CREE. The total power of the module is 210W. Considering the total output current of the constant-current driver, the performance of the DTM is analyzed, and the following assumptions are made:

- Each switching device is an ideal device without considering the parasitic parameters of MOSFET and diode.

- All LEDs are ideal components with the same parameters, and their equivalent resistance is not affected by temperature.
- The selection of 200kHz switching frequency is a comprehensive consideration of realizability, low ripple, low conducted interference, miniaturization, long life, high efficiency and other factors for the LED driver.

Considering practical application needs, the constant-current driver is selected to operate in two states. First, when the minimum input voltage is 325V, the full-load output current is 4.5A, and the output voltage is 48V. Secondly, when the highest input voltage is 445V, the lowest output current is 0.75A and the output voltage is 37V. Operating condition, circuit component, and static operating points are shown in TABLE 3. Where, the static operating points are calculated by Formula (2).

By replacing component parameters, operating conditions and static operating points with Equation (3), the state-space average small-signal open-loop transfer function from duty ratio to inductance current and LED current corresponding to the two static operating points can be obtained respectively, as shown in TABLE 4.

TABLE 3. Component parameters.

ITEM	PARAMETERS
Operating condition	$U_s = 325 \sim 445V, n = 3, T_J = 85°C,$ $T_s = 5 \times 10^{-6}s, u_{r\,max} = 5V, f_s = 200\,kHz,$ $I_{LED} = 0.75 \sim 4.5A, U_{LED} = 37 \sim 48V,$ $R_{LED} = 49.333 \sim 10.667\,\Omega$
Circuit component	$C_c = 0.12\,\mu F(R_{Cc} = 1.327\Omega),$ $L_m = 23.7\,\mu H, R_{Ls} = R_{LEDs} = 0.01\Omega,$ $L_f = 88\,\mu H(R_{Lf} = 0.12\Omega),$ $C_f = 66\,\mu F(R_{Cf} = 0.002\Omega)$
Operating point 1	$U_s = 325V, U_{LED} = 48V,$ $I_{LED} = 4.5A, R_{LED} = 10.667\Omega,$ $D = 0.348, U_{Cc} = 113.1V,$ $I_m = 0.456A, I_L = 4.5A,$ $U_{Cf} = 48V$
Operating point 2	$U_s = 445V, U_{LED} = 37V,$ $I_{LED} = 0.75A, R_{LED} = 49.333\,\Omega,$ $D = 0.147, U_{Cc} = 65.415V,$ $I_m = 0.177A, I_L = 0.75A,$ $U_{Cf} = 37.052V$

In order to simplify the calculation of exponential matrix, the discrete time small signal transfer function is obtained in three steps. First, the values of coefficient matrices such as $\mathbf{A_0}$, $\mathbf{A_1}$, $\mathbf{B_0}$, $\mathbf{B_1}$, $\mathbf{C_0}$, $\mathbf{C_1}$, $\mathbf{E_0}$ and $\mathbf{E_1}$ are calculated by substituting the parameters. Then, the exponential matrix in $\mathbf{\Phi}$ and $\mathbf{\gamma}$ is replaced by the first-order Taylor expansion shown in Formula (11), and the values are calculated. Finally, put the calculated $\mathbf{\Phi}$ and $\mathbf{\gamma}$ values into Formula (10) to obtain the discrete-time small-signals open-loop pulse transfer functions from duty ratio to inductance current and LED current corresponding to the two static operating points in three modulations respectively, as shown in TABLE 5.

B. COMPARISON OF THE PROPOSED DTM WITH THE DAM

Bode Diagram comparison of DAM and DTM is shown in Figure 4 and Figure 5, where, the DAMs are obtained by discretizing the state-average small-signal open-loop transfer functions. In the figures, Ld and LEDd represent the transfer function from duty ratio to inductance current and to LED current respectively. S represents the discrete average model, while T, L and D represent the DTMs corresponding to the Trailing-edge, Leading-edge and Double-edge modulation respectively. 1 and 2 represent two types of operation states. Exact is the measured waveform.

Figure 4 shows the Bode diagram of the DAM and the DTMs when output is 4.5A/48V. It can be seen that the amplitude-frequency characteristics of the DTM and the DAM deviate significantly at the resonance peak and after 50kHz, as shown in TABLE 6. This further indicates that the state-space small signal model is not accurate enough to characterize the resonance peak and high-frequency band. In addition, compared with Trailing-edge and Double-edge modulation, when the AHBC is modulated by Leading-edge, the amplitude of inductance current has a large deviation in the low frequency band and the phase of LED current has a larger lag in the high frequency band.

Figure 5 shows the Bode diagram of the DAM and the DTMs when output is 0.75A/37V. It can be seen that under light load, the amplitude-frequency characteristics of the inductance current also have a large deviation in the low-frequency component under the three modes of modulation, except for the great difference between the resonant peak and the high frequency, as shown in TABLE 6. It can also be seen that DTM is very accurate in describing the dynamic characteristics of LED current, especially the DTMT and DTMD.

As also can be seen from TABLE 6, compared with full load, amplitude-frequency characteristics are different in the whole frequency band when output is under light load, and the resonance peak value obviously increases. This shows the influence of static operating points on small-signal dynamic models.

Figure 6 shows the root locus of the discrete model corresponding to operating point 1. Where, (a) to (d), (e) to (h) are discrete models of duty ratio to inductance current and duty ratio to LED current respectively. (a) and (e) are based on the state-space average method, but (b) to (d) and (f) to (h) are respectively based on discrete-time modeling in three modulation modes. It can be seen that the impulse

TABLE 4. State average small-signal model.

OPERATING POINT	SSA
Operating point 1 (48V/4.5A)	$G_{i_L d1}(s) = \dfrac{5.9559\,(7.0472 \times 10^{-4}s + 1)(1.4421 \times 10^{-12}s^2 + 2.7418 \times 10^{-7}s + 1)}{(5.6948 \times 10^{-9}s^2 + 2.5461 \times 10^{-5}s + 1)(2.8361 \times 10^{-12}s^2 + 1.6347 \times 10^{-7}s + 1)}$ $G_{i_{LED}d1}(s) = \dfrac{5.9564\,(7.9177 \times 10^{-7}s + 1)(1.4421 \times 10^{-12}s^2 + 2.7418 \times 10^{-7}s + 1)}{(5.6948 \times 10^{-9}s^2 + 2.5461 \times 10^{-5}s + 1)(2.8361 \times 10^{-12}s^2 + 1.6347 \times 10^{-7}s + 1)}$
Operating point 2 (37V/0.75A)	$G_{i_L d2}(s) = \dfrac{4.2217\,(3.3 \times 10^{-3}s + 1)(1.4421 \times 10^{-12}s^2 + 1.7676 \times 10^{-7}s + 1)}{(5.872 \times 10^{-9}s^2 + 1.5473 \times 10^{-5}s + 1)(2.8019 \times 10^{-12}s^2 + 1.6352 \times 10^{-7}s + 1)}$ $G_{i_{LED}d2}(s) = \dfrac{4.2224\,(7.9177 \times 10^{-7}s + 1)(1.4421 \times 10^{-12}s^2 + 1.7676 \times 10^{-7}s + 1)}{(5.872 \times 10^{-9}s^2 + 1.5473 \times 10^{-5}s + 1)(2.8019 \times 10^{-12}s^2 + 1.6352 \times 10^{-7}s + 1)}$

TABLE 5. Small-signal DTMs corresponding to the three modes of modulation.

MODULATION	OPERATING POINT	DTM
Trailing-edge modulation	operating point 1 ($t_d = 3\mu s$)	$G_{i_L dT1}(z) = \dfrac{\hat{i}_L(z)}{\hat{d}(z)} = \dfrac{4.2667\,(z+3.686\,)(z+1.204\,)(z-0.9934\,)}{(z^2 - 2.015\,z + 1.019\,)(z^2 + 3.737\,z + 6.752\,)}$
		$G_{i_{LED} dT1}(z) = \dfrac{\hat{i}_{LED}(z)}{\hat{d}(z)} = \dfrac{0.012817\,(z+0.075)(z^2 + 5.439\,z + 16.03)}{(z^2 - 2.015\,z + 1.019)(z^2 + 3.737\,z + 6.752\,)}$
	operating point 1 ($t_d = 2\mu s$)	$G_{i_L dT2}(z) = \dfrac{\hat{i}_L(z)}{\hat{d}(z)} = \dfrac{7.7993\,(z+5.744)(z+1.419)(z-0.9993)}{(z^2 - 1.998\,z + 1.002)(z^2 + 3.004\,z + 7.01)}$
		$G_{i_{LED} dT2}(z) = \dfrac{\hat{i}_{LED}(z)}{\hat{d}(z)} = \dfrac{0.0075702\,(z+0.1403)(z^2 + 5.211\,z + 16.33)}{(z^2 - 1.998\,z + 1.002)(z^2 + 3.004\,z + 7.01)}$
Leading-edge modulation	operating point 1 ($t_d = 4\mu s$)	$G_{i_L dL1}(z) = \dfrac{\hat{i}_L(z)}{\hat{d}(z)} = \dfrac{0.70845\,(z-0.9914\,)(z^2 + 12.45\,z + 41.44\,)}{(z^2 - 2.013\,z + 1.017\,)(z^2 + 2.568\,z + 6.8\,)}$
		$G_{i_{LED} dL1}(z) = \dfrac{\hat{i}_{LED}(z)}{\hat{d}(z)} = \dfrac{0.00081723\,(z+13.2)(z^2 + 3.767\,z + 19.14\,)}{(z^2 - 2.013\,z + 1.017\,)(z^2 + 2.568\,z + 6.8\,)}$
	operating point 2 ($t_d = 4.5\mu s$)	$G_{i_L dL2}(z) = \dfrac{\hat{i}_L(z)}{\hat{d}(z)} = \dfrac{4.8927\,(z-0.9979)(z^2 + 2.558\,z + 17.34)}{(z^2 - 1.998\,z + 1.002\,)(z^2 + 0.488\,z + 7.766\,)}$
		$G_{i_{LED} dL2}(z) = \dfrac{\hat{i}_{LED}(z)}{\hat{d}(z)} = \dfrac{0.001904\,(z+3.626)(z^2 + 0.9309\,z + 15.91)}{(z^2 - 1.998\,z + 1.002\,)(z^2 + 0.488\,z + 7.766\,)}$
Double-edge modulation	operating point 1 ($t_d = 2.5\mu s$)	$G_{i_L dD1}(z) = \dfrac{\hat{i}_L(z)}{\hat{d}(z)} = \dfrac{4.9578\,(z-0.9932)(z^2 + 3.825\,z + 3.962\,)}{(z^2 - 2.015\,z + 1.019\,)(z^2 + 3.821\,z + 6.722\,)}$
		$G_{i_{LED} dD1}(z) = \dfrac{\hat{i}_{LED}(z)}{\hat{d}(z)} = \dfrac{0.0074818\,(z+0.1306)(z^2 + 9.969\,z + 25.28)}{(z^2 - 2.015\,z + 1.019\,)(z^2 + 3.821\,z + 6.722\,)}$
	operating point 2 ($t_d = 2.5\mu s$)	$G_{i_L dD2}(z) = \dfrac{\hat{i}_L(z)}{\hat{d}(z)} = \dfrac{8.6519\,(z+4.047)(z+2.125)(z-0.9989\,)}{(z^2 - 1.998\,z + 1.002\,)(z^2 + 3.514\,z + 7.252\,)}$
		$G_{i_{LED} dD2}(z) = \dfrac{\hat{i}_{LED}(z)}{\hat{d}(z)} = \dfrac{0.0060451\,(z+0.3109)(z^2 + 6.84\,z + 18.53)}{(z^2 - 1.998\,z + 1.002\,)(z^2 + 3.514\,z + 7.252\,)}$

(a) Transfer function from duty ratio to inductive current

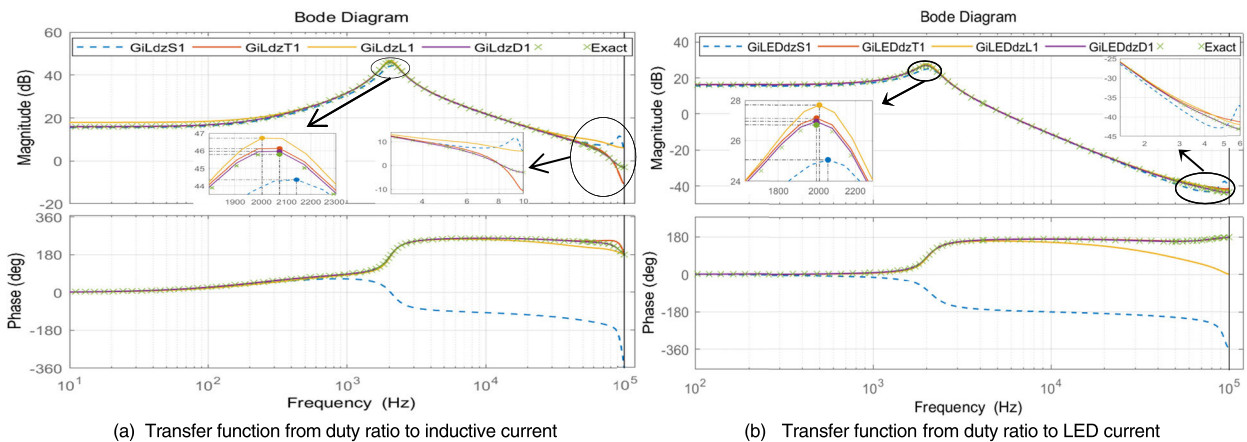(b) Transfer function from duty ratio to LED current

FIGURE 4. Bode diagram comparison of DTM and DAM at the point of 325V input and 4.5A/48V output.

transfer function established by the discrete-time modeling is no longer stable because the loop delay is taken into account. This further confirms the effect of delay on the stability of the open-loop system.

In this section, the DTMs, DAM and measured characteristics of two operating points with three modulations are compared. The results show that the DTMs can better represent the real dynamic characteristics of the converter than the DAM. Especially in the resonant peak and high frequency band, DTMT and DTMD can well match the measured characteristics.

V. PERFORMANCE OF AVERAGE CURRENT-MODE CONTROL

Considering the average current mode has better closed-loop control performance. In this section, the average current mode compensators are designed based on SSA to verify the correctness of the DTMs.
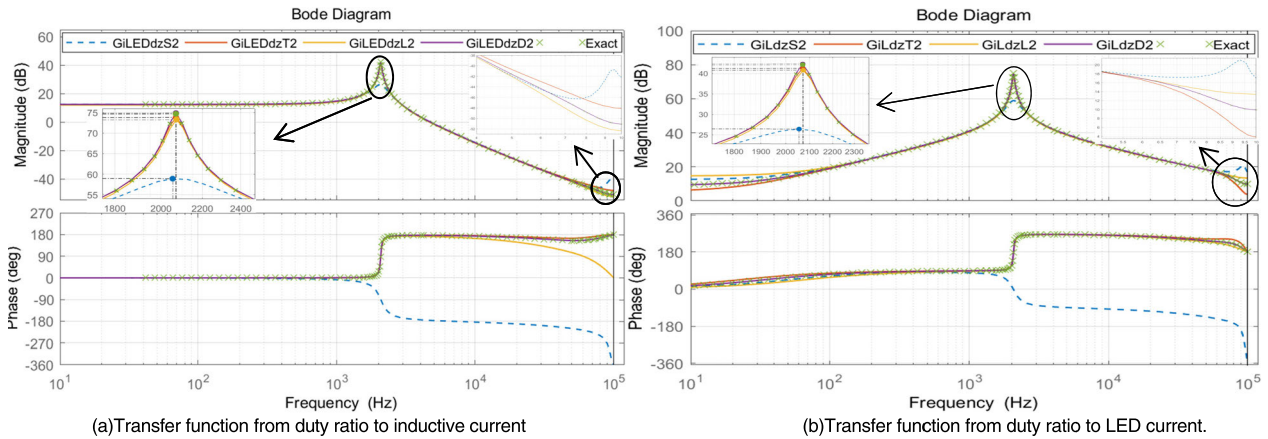
(a)Transfer function from duty ratio to inductive current

(b)Transfer function from duty ratio to LED current.

FIGURE 5. Bode diagram comparison of DTM and DAM at the point of 445V input and 0.75A/37V output.

TABLE 6. Comparison of resonant peak and high frequency characteristics of discrete model.

OPERATING POINT	MODEL	$G_{i_L d}(z)$					$G_{i_{LED} d}(z)$				
		Resonance Peak			Characteristics at 95kHz		Resonance Peak			Characteristics at 95kHz	
		Frequency (kHz)	Amplitude (dB)	Phase (°)	Amplitude (dB)	Phase (°)	Frequency (kHz)	Amplitude (dB)	Phase (°)	Amplitude (dB)	Phase (°)
OPERATING POINT 1	DAM	2.14	44.4	-13	10.07	-259	2.05	25.1	-80.9	-37.1	-315
	DTMT	2.07	46.1	176	-8.38	219	1.99	27.1	80.5	-41.3	179
	DTML	2	46.7	161	6.18	186	2	27.8	75.1	-42.1	10.6
	DTMD	2.07	46	180	-2.65	194	1.99	27	80.5	-43.3	179
	Exact	2.07	45.8	180	-2.7	192	1.99	26.8	80.5	-43.2	179
OPERATING POINT 2	DAM	2.06	58.9	2.5	21.1	-229	2.06	26.5	-80.9	-40.8	-320
	DTMT	2.07	73.8	176	5.39	212	2.07	41.2	80.5	-48	179
	DTML	2.07	73.3	175	13.6	189	2.07	40.7	75.1	-52.2	13.2
	DTMD	2.07	74.8	176	10.4	197	2.07	42.3	80.5	-50.9	176
	Exact	2.07	74.6	176	10.3	196	2.07	42.1	80.5	-50.7	176

A. DESIGN OF AVERAGE CURRENT MODE COMPENSATOR BASED ON SSA

Figure 7 is the average current mode control block diagram of the converter. In the figure, $G_{i_L d}(s)$ and $G_{i_{LED} d}(s)$ are transfer functions from duty cycle to inductance current and LED current. $G_{PWM}(s)$ is the modulator transfer function. $H_{i_L}(s)$ and $H_{i_{LED}}(s)$ are feedback gains. $G_{ci_L}(s)$ and $G_{ci_{LED}}(s)$ are inductance current and LED current compensators respectively.

The gain of inductance current inner loop and LED current outer loop are shown in Equations (12) and (13) respectively.

$$T_{i_L}(s) = G_{ci_L}(s)G_{PWM}(s)H_{i_L}(s)G_{i_L d}(s) \tag{12}$$

$$T_{i_{LED}}(s) = G_{ci_{LED}}(s)\frac{H_{i_{LED}}(s)}{H_{i_L}(s)} \frac{G_{i_{LED} d}(s)}{G_{i_L d}(s)} \frac{T_{i_L}(s)}{1+T_{i_L}(s)} \tag{13}$$

Because the inductance current inner loop bandwidth is generally designed to be very wide, that is, $\omega \ll \omega_{ci_L}$, so $T_{i_L}(s)/(1+T_{i_L}(s)) \approx 1$. Thus

$$T_{i_{LED}}(s) \approx G_{ci_{LED}}(s)\frac{H_{i_{LED}}}{H_{i_L}} \frac{G_{i_{LED} d}(s)}{G_{i_L d}(s)} \tag{14}$$

After normalization of $G_{PWM}(s)$, $H_{i_L}(s)$ and $H_{i_{LED}}(s)$, the loop gain of inner loop and outer loop without correction

are respectively

$$T_{di_L}(s) = G_{i_L d}(s) \tag{15}$$

$$T_{di_{LED}}(s) \approx \frac{G_{i_{LED} d}(s)}{G_{i_L d}(s)} \tag{16}$$

The inductance current inner loop is compensated by two poles and one zero point controller.

$$G_{ci_L}(s) = \frac{K_{ci_L}(1 + s/\omega_{zci_L})}{s(1 + s/\omega_{pci_L})} \tag{17}$$

The parameters for $G_{ci_L}(s)$ can be selected as follows:

- Place ω_{zci_L} as high as possible, yet not exceeding ω_{d1}.
- Place ω_{pci_L} at half the switching frequency to eliminate the switching ripple noise.
- Adjust K_{ci_L} to place the crossover frequency of $T_{di_L}(s)$ at 1/10 of the switching frequency, i.e., 20kHz.

The LED current outer loop is compensated by two poles and one zero point controller.

$$G_{ci_{LED}}(s) = \frac{K_{ci_{LED}}(1 + s/\omega_{zci_{LED}})}{s(1 + s/\omega_{pci_{LED}})} \tag{18}$$

The parameters for $G_{ci_{LED}}(s)$ can be selected as follows:
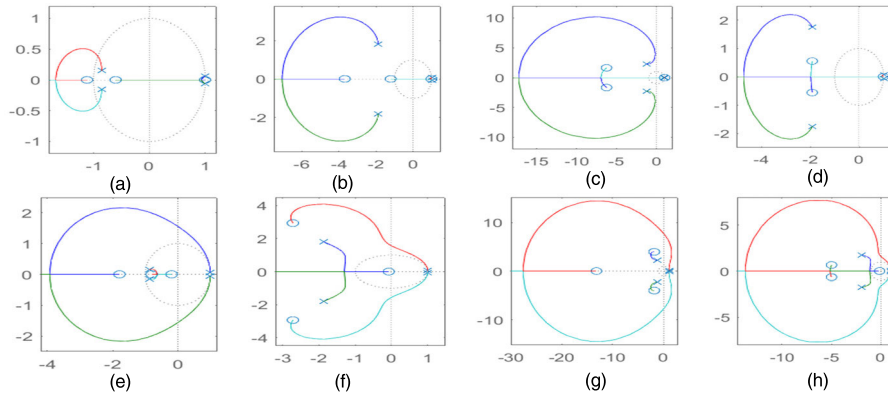
FIGURE 6. Root locus comparison of operating point 1: (a) to (d) are transfer functions from duty ratio to inductive current; (e) to (h) are transfer functions from duty ratio to LED current; (a) and (e) are based on the state-space average method; (b) to (d) and (f) to (h) are respectively based on the discrete-time modeling in three modulation modes.
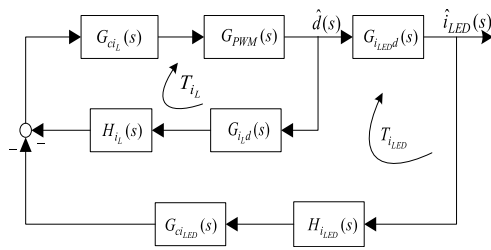
FIGURE 7. Average current mode control block diagram of the converter.

- Place $\omega_{zci_{LED}}$ close to the lowest descent frequency of $T_{di_{LED}}(s)$.
- Place $\omega_{pci_{LED}}$ at half the switching frequency to eliminate the switching ripple noise.
- Adjust $K_{ci_{LED}}$ to place the crossover frequency of $T_{di_{LED}}(s)$ at 1/200 of the switching frequency, i.e., 1kHz.

B. ANALYSIS OF CONTROL PERFORMANCE BASED ON DTMs

When the inductance current inner loop compensator of operating point 1 and point 2 are shown in Equation (19) and

Equation (20).

$$G_{ciL1}(s) = \frac{2120(1 + s/\sqrt{1.6 \times 10^8})}{s(1 + s/628000)} \quad (19)$$

$$G_{ciL2}(s) = \frac{665(1 + s/\sqrt{1.6 \times 10^8})}{s(1 + s/628000)} \quad (20)$$

As shown in Figure 8 and Figure 9. After compensation, for operating point 1, the inductance current inner loop gain margin(GM) of DAM, DTMT, DTML and DTMD are 1.86dB, -29.9dB, -29.9dB, and -29.8dB, respectively, and, for operating point 2, the GM are 2.59dB, -48dB, -47.2dB, and -49 dB, respectively.

When the LED current outer loop compensator of operating point 1 and point 2 are shown in Equation (21) and Equation (22).

$$G_{ci_{LED}1}(s) = \frac{6230(1 + s/1400)}{s(1 + s/628000)} \quad (21)$$

$$G_{ci_{LED}2}(s) = \frac{6150(1 + s/300)}{s(1 + s/628000)} \quad (22)$$

As shown in Figure 10 and 11. After compensation, for operating point 1 and point 2, the DAM based closed-loop
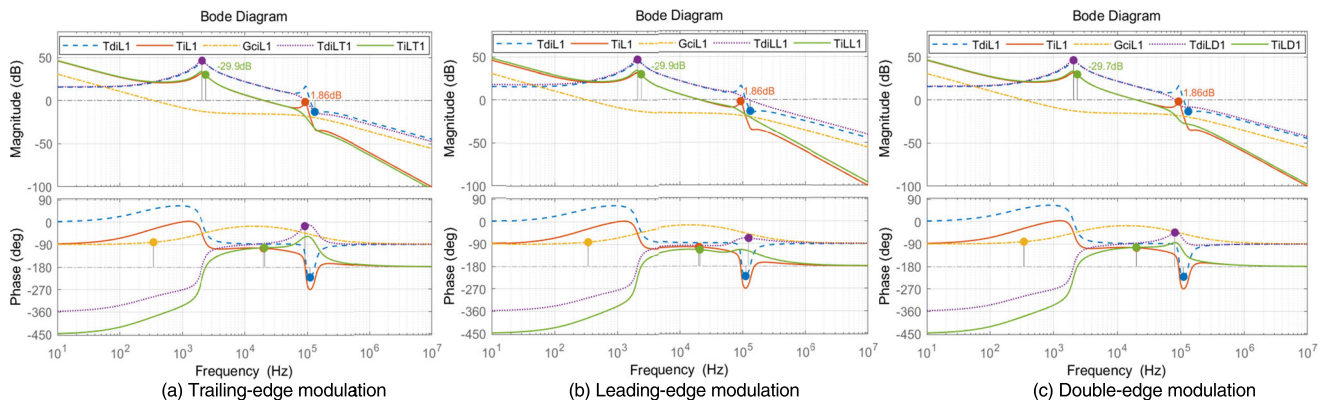
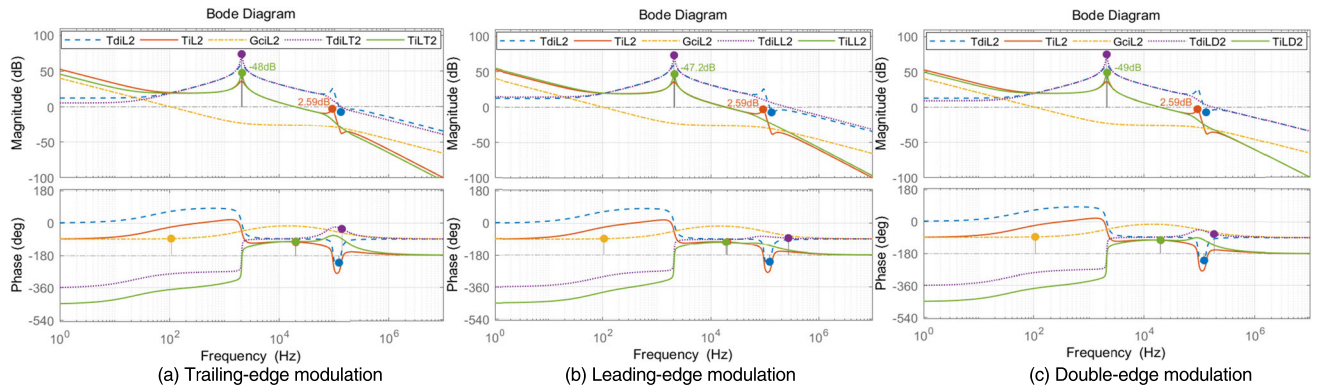**FIGURE 8.** Bode diagrams of inductive current inner loop gain of operating point 1.

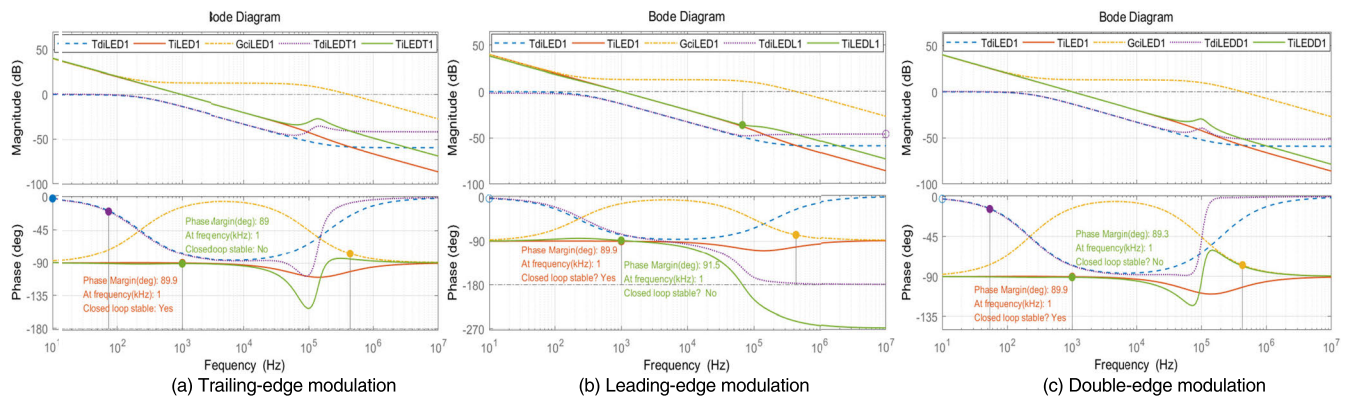**FIGURE 9.** Bode diagrams of inductive current inner loop gain of operating point 2.

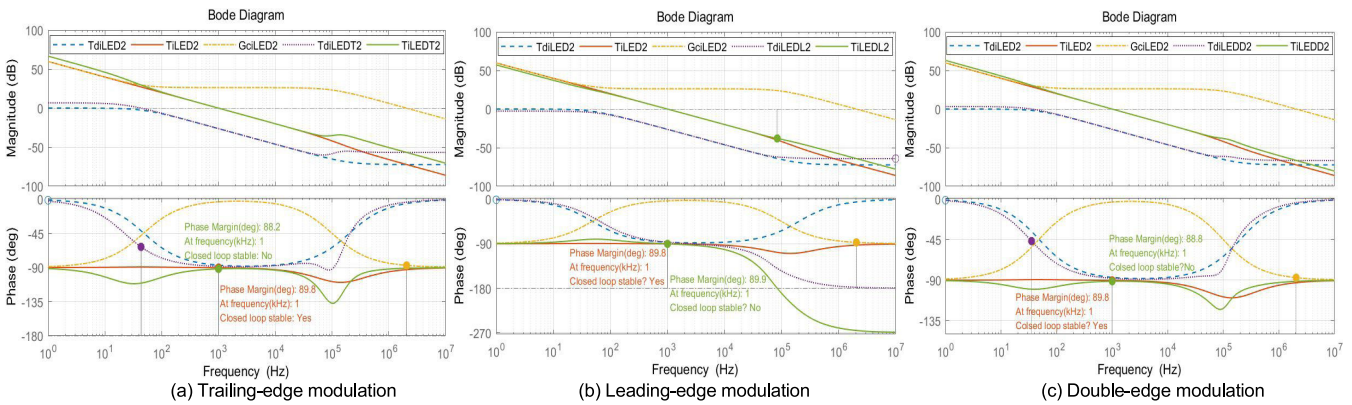**FIGURE 10.** Bode diagrams of LED current outer loop gain of operating point 1.

FIGURE 11. Bode diagrams of LED current outer loop gain of operating point 2.

system is stable, but the closed loop systems based on DTMT, DTML and DTMD are all unstable.

By analyzing the gain of the loop before compensation, it can be seen that the control loop based on DTMs become a non-minimum phase system due to the introduction of delay. As shown in Equation (23) and Equation (24), the inductance current inner loop has four positive real part poles and two positive real part zeros. The approximated LED current outer loop contains two positive real part poles and

two positive real part zeros, as shown in Equation (25) and Equation (26). Therefore, as shown in Figures 12(a), 12(c), 13(a) and 13(c), when the SSA-based designed compensators are used for analog average current mode control, the converter is stable and has a good control effect. In the performance test of the analog control, we add the load disturbance, and the output current can quickly recover to a stable state after the converter is short connected with three LED lamp beads during stable operating. However, as shown

$$T_{di_L T1}(s) = \frac{2.6857 \times 10^5 (s + 1331)(s^2 - 4.528 \times 10^5 s + 7.386 \times 10^{11})}{(s^2 - 3727s + 1.63 \times 10^8)(s^2 - 3.82 \times 10^5 s + 2.618 \times 10^{11})} \tag{23}$$

$$T_{di_L T2}(s) = \frac{7.0087 \times 10^5 (s + 139.8)(s^2 - 8.81 \times 10^5 s + 7.475 \times 10^{11})}{(s^2 - 472.1s + 1.694 \times 10^8)(s^2 - 3.895 \times 10^5 s + 2.27 \times 10^{11})} \tag{24}$$

$$T_{di_{LED} T1}(s) \approx \frac{0.00856(s + 4.691 \times 10^5)(s^2 - 5.893 \times 10^5 s + 5.893 \times 10^{11})}{(s + 1331)(s^2 - 4.528 \times 10^5 s + 7.386 \times 10^{11})} \tag{25}$$

$$T_{di_{LED} T2}(s) \approx \frac{0.0014495(s + 5.746 \times 10^5)(s^2 - 6.155 \times 10^5 s + 2.745 \times 10^{11})}{(s + 139.8)(s^2 - 8.81 \times 10^5 s + 7.475 \times 10^{11})} \tag{26}$$

(a) Analog controlled of operating point 1 (b) Digital controlled of operating point 1 (c) Analog controlled of operating point 2 (d) Digital controlled of operating point 2
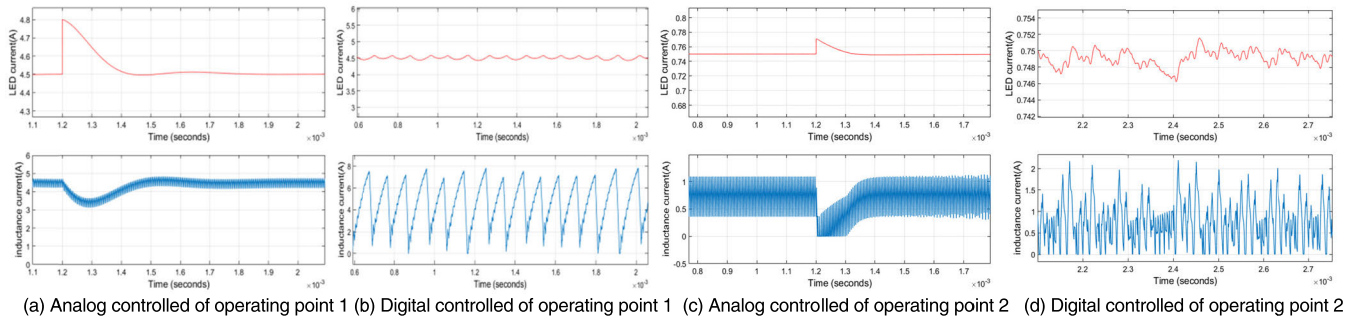
FIGURE 12. Simulation results of analog and digital average current mode controlled converters with double-edge modulation.

(a) Analog controlled of operating point 1 (b) Digital controlled of operating point 1 (c) Analog controlled of operating point 2 (d) Digital controlled of operating point 2
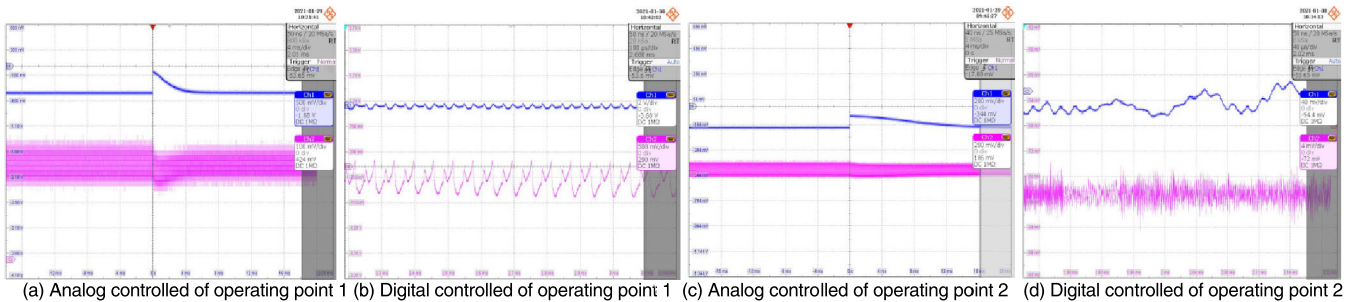
FIGURE 13. Experiment results of analog and digital average current mode controlled converters with double-edge modulation.

in Figures 12(b), 12(d), 13(b) and 13(d), the converter is no longer stable when they are used for digital average current mode control. This further proves that the DTMs can more truly describe the real digital control characteristics of the converter (23)–(26), as shown at the top of the page.

The design of digital controller based on DTMs needs to be further studied, which is one of the key works of our team in the next step, and we hope to design a digital controller with excellent performance. Possible control algorithms include predictive current control, deadbeat control, fuzzy PID control and some other advanced control methods.

In this section, the compensators of the converter are designed based on SSA. Simulation and experiment show that the converter can achieve good control performance when the compensators are used for analog control, but the converter can't run stably because of loop delay when they are used

for digital control. This further demonstrates the accuracy of DTMs.
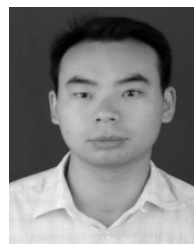
VI. CONCLUSION
In this paper, the discrete-time small-signal model at different operating points and input conditions was established for AHBC LED constant-current driver with Trailing-edge, Leading-edge and Double-edge modulation. The effects of parasitic resistance, load characteristics, sampling effect, modulation effect and loop delay were considered. The complex matrix exponential operation was calculated by first order approximation and directly substituted into the data. Simulation and experimental results show that the proposed DTMs can more accurately characterize the resonant peak and high-frequency dynamic characteristics, and are very suitable for the design of high-frequency digital controller. We will continue to work hard to design a digital

controller with excellent performance based on the proposed DTMs.

REFERENCES

[1] K. Ramakrishnareddy Ch, S. Porpandiselvi, and N. Vishwanathan, "An efficient ripple-free LED driver with zero-voltage switching for street lighting applications," *EPE J.*, vol. 29, no. 3, pp. 120–131, Jul. 2019, doi: 10.1080/09398368.2019.1570745.

[2] J. Bhardwaj, J. M. Cesaratto, I. H. Wildeson, H. Choy, A. Tandon, W. A. Soer, P. J. Schmidt, B. Spinger, P. Deb, O. B. Shchekin, and W. Götz, "Progress in high-luminance LED technology for solid-state lighting," *Phys. Status Solidi (A)*, vol. 214, no. 8, Aug. 2017, Art. no. 1600826, doi: 10.1002/pssa.201600826.

[3] P. Fang, S. Webb, Y. Chen, Y.-F. Liu, and P. C. Sen, "A multiplexing ripple cancellation LED driver with true single-stage power conversion and flicker-free operation," *IEEE Trans. Power Electron.*, vol. 34, no. 10, pp. 10105–10120, Oct. 2019, doi: 10.1109/TPEL.2019.2892981.

[4] Y. HuangC Li and Y. Chen, "A modified asymmetrical half-bridge flyback converter for step-down AC–DC applications," *IEEE Trans. Power Electron.*, vol. 35, no. 5, pp. 4613–4621, May 2020, doi: 10.1109/TPEL.2019.2940322.

[5] C.-Y. Ting, Y.-C. Hsu, J.-Y. Lin, and C.-P. Chen, "A single-stage asymmetrical half-bridge flyback converter with resonant operation," *Energies*, vol. 11, no. 7, p. 1721, Jul. 2018, doi: 10.3390/en11071721.

[6] R. Kathiresan, P. Das, T. Reindl, and S. K. Panda, "Novel high-power non-resonant multichannel LED driver," *IEEE Trans. Ind. Electron.*, vol. 64, no. 7, pp. 5851–5864, Jul. 2017, doi: 10.1109/TIE.2017.2652396.

[7] E. Mujjalinvimut, P. Navaratana Na Ayudhya, and A. Sangswang, "An improved asymmetrical half-bridge converter with self-driven synchronous rectifier for dimmable LED lighting," *IEEE Trans. Ind. Electron.*, vol. 63, no. 2, pp. 913–925, Feb. 2016, doi: 10.1109/TIE.2015.2477263.

[8] M. Arias, M. Fernandez Diaz, J. E. Rodriguez Cadierno, D. G. Lamar, and J. Sebastian, "Digital implementation of the feedforward loop of the asymmetrical half-bridge converter for LED lighting applications," *IEEE J. Emerg. Sel. Topics Power Electron.*, vol. 3, no. 3, pp. 642–653, Sep. 2015, doi: 10.1109/JESTPE.2015.2428291.

[9] X. Zhang, R. Min, D. Lyu, D. Zhang, and Y. Wang, "Current tracking delay effect minimization for digital peak current mode control of DC–DC boost converter," *IEEE Trans. Power Electron.*, vol. 34, no. 12, pp. 12384–12395, Dec. 2019, doi: 10.1109/TPEL.2019.2905864.

[10] Y. QiuH Liu and X. Chen, "Digital average current-mode control of PWM DC–DC converters without current sensors," *IEEE Trans. Ind. Electron.*, vol. 57, no. 5, pp. 1670–1677, May 2010, doi: 10.1109/TIE.2009.2032130.

[11] E. Meyer and Y.-F. Liu, "Digital charge balance controller with an auxiliary circuit for improved unloading transient performance of buck converters," *IEEE Trans. Power Electron.*, vol. 28, no. 1, pp. 357–370, Jan. 2013, doi: 10.1109/TPEL.2012.2198923.

[12] B. Choi, W. Lim, S. Choi, and J. Sun, "Comparative performance evaluation of current-mode control schemes adapted to asymmetrically driven bridge-type pulsewidth modulated DC-to-DC converters," *IEEE Trans. Ind. Electron.*, vol. 55, no. 5, pp. 2033–2042, May 2008, doi: 10.1109/TIE.2008.920582.

[13] J. D. van Wyk and F. C. Lee, "On a future for power electronics," *IEEE J. Emerg. Sel. Topics Power Electron.*, vol. 1, no. 2, pp. 59–72, Jun. 2013, doi: 10.1109/JESTPE.2013.2271499.

[14] D. Sype, K. D. Gussemé, A. Bossche, and J. A. Melkebeek, "Small-signal Laplace-domain analysis of uniformly-sampled pulse-width modulators," in *Proc. IEEE 35th Annu. Power Electron. Spec. Conf.*, vol. 6, Jun. 2004, pp. 4292–4298, doi: 10.1109/PESC.2004.1354760.

[15] A. V. Peterchev and S. R. Sanders, "Quantization resolution and limit cycling in digitally controlled PWM converters," *IEEE Trans. Power Electron.*, vol. 18, no. 1, pp. 301–308, Jan. 2003, doi: 10.1109/tpel.2002.807092.

[16] D. Maksimovic and R. Zane, "Small-signal discrete-time modeling of digitally controlled PWM converters," *IEEE Trans. Power Electron.*, vol. 22, no. 6, pp. 2552–2556, Nov. 2007, doi: 10.1109/TPEL.2007.909776.

[17] J. Sebastian, J.A. Cobos, O. Garcia, and J. Uceda, "Small-signal modelling of the half-bridge complementary-control DC-to-DC converter," in *Proc. IV IEEE Int. Power Electron. Congr.*, Oct. 1995, pp. 44–50.

[18] S. Abedinpour, R. Liu, G. Fasullo, and K. Shenai, "Small-signal analysis of a new asymmetrical half-bridge DC-DC converter," in *Proc. IEEE 31st Annu. Power Electron. Spec. Conf.*, Jun. 2000, pp. 843–847.

[19] B. Choi, W. Lim, S. Bang, and S. Choi, "Small-signal analysis and control design of asymmetrical half-bridge DC-DC converters," *IEEE Trans. Ind. Electron.*, vol. 53, no. 2, pp. 511–520, Apr. 2006, doi: 10.1109/TIE.2006.870715.

[20] L. Yao, J. A. Abu-Qahouq, and I. Batarseh, "Unified analog and digital models for half bridge DC-DC converter with current doubler rectifier," in *Proc. 20th Annu. IEEE Appl. Power Electron. Conf. Expo. (APEC)*, May 2005, pp. 1386–1392.

[21] D.J. Packard, "Discrete modeling and analysis of switching regulators," California Inst. Technol., Pasadena, CA, USA, Tech. Rep., 1976.

[22] F. Huliehel and S. Ben-Yaakov, "Low-frequency sampled-data models of switched mode DC-DC converters," *IEEE Trans. Power Electron.*, vol. 6, no. 1, pp. 55–61, Jan. 1991, doi: 10.1109/63.65003.

[23] D. Maksimovic and R. Zane, "Small-signal discrete-time modeling of digitally controlled DC-DC converters," in *Proc. IEEE Workshops Comput. Power Electron.*, 2006, pp. 231–235, doi: 10.1109/COMPEL.2006.305680.

[24] D. M. VandeSype, K. DeGusseme, F. M. L. L. DeBelie, A. P. VandenBossche, and J. A. Melkebeek, "Small-signal *z*-domain analysis of digitally controlled converters," *IEEE Trans. Power Electron.*, vol. 21, no. 2, pp. 470–478, Mar. 2006, doi: 10.1109/TPEL.2005.869758.

[25] V. Rajasekaran, J. Sun, and B. S. Heck, "Bilinear discrete-time modeling for enhanced stability prediction and digital control design," *IEEE Trans. Power Electron.*, vol. 18, no. 1, pp. 381–389, Jan. 2003, doi: 10.1109/TPEL.2002.807167.

[26] X. Li, X. Ruan, Q. Jin, M. Sha, and C. K. Tse, "Approximate discrete-time modeling of DC–DC converters with consideration of the effects of pulse width modulation," *IEEE Trans. Power Electron.*, vol. 33, no. 8, pp. 7071–7082, Aug. 2018, doi: 10.1109/TPEL.2017.2752419.

[27] M. Leng, G. Zhou, S. Zhou, K. Zhang, and S. Xu, "Stability analysis for peak current-mode controlled buck LED driver based on discrete-time modeling," *IEEE J. Emerg. Sel. Topics Power Electron.*, vol. 6, no. 3, pp. 1567–1580, Sep. 2018, doi: 10.1109/JESTPE.2017.2781361.

ZHIYONG QIAO was born in 1978. He received the M.S. degree in control theory and control engineering from Xinjiang University, Urumqi, China, in 2008. He is currently pursuing the Ph.D. degree with the Graduate School, Southwest University of Science and Technology, Mianyang. He is also an Associate Professor with the Department of Information Engineering, Mianyang Polytechnic, Mianyang. His current research interests include power electronics conversion technology, embedded system design, and digital control technology.

SHUNLI WANG (Student Member, IEEE) was born in 1985. He is currently a Professor, a Master Tutor, a Young Scholar, and a Leading Expert on new energy research, the DTLab Head, and the New Energy Measurement and Control Research Team Leader. He conducted measurement and control processing on the needs of high power Li-ion battery field for its modeling and state estimation strategy. He has undertaken more than 40 projects and holds 20 patents. He has published more than 60 articles on world famous journals, such as *Journal of Power Sources*. He received 20 awards, including the Science and Technology Progress Award and the University and Enterprise Innovation Talent Team. He developed multiple generation systems for battery packs, improving the aircraft reliability and expanding its application fields with significant social and economic benefits.

RONGHAI WANG was born in 1969. He is currently a Professor, mainly engaged in the research of industrial control.

NAN ZHANG was born in 1971. He is currently a Senior Engineer. He is mainly engaged in the research of special power converter.

YILE SHI was born in 1996. He is currently pursuing the master's degree. He is mainly engaged in the research of DC–DC converter.

XIN XIONG was born in 1995. He is currently pursuing the master's degree with the Southwest University of Science and Technology. By focusing on the measurement and control requirements in the new energy field, he conducted the research on the energy management of power lithium-ion battery packs, including the signal detection, estimation on the complex energy supply systems, and the core automated detection and control technology formed for the lithium-ion battery packs.

ZHIGUI LIU was born in 1966. He is currently the Executive Dean of the Graduate School, Southwest University of Science and Technology, a Doctoral Supervisor with the School of Information Engineering, Southwest University of Science and Technology, and a Professor. His research interests include control theory and control engineering.

● ● ●